Correspondence to:
G. L. Delzanno,
delzanno@lanl.gov

Future beam experiments in the magnetosphere with plasma contactors: How do we get the charge off the spacecraft?

G. L. Delzanno[1], J. E. Borovsky[2,3], M. F. Thomsen[4], J. D. Moulton[1], and E. A. MacDonald[5]

[1]Theoretical Division, Los Alamos National Laboratory, Los Alamos, New Mexico, USA, [2]Space Science Institute, Boulder, Colorado, USA, [3]AOSS, University of Michigan, Ann Arbor, Michigan, USA, [4]Intelligence and Space Research Division, Los Alamos National Laboratory, Los Alamos, New Mexico, USA, [5]Nasa Goddard, Greenbelt, Maryland, USA

Abstract The idea of using a high-voltage electron beam with substantial current to actively probe magnetic field line connectivity in space has been discussed since the 1970s. However, its experimental realization onboard a magnetospheric spacecraft has never been accomplished because the tenuous magnetospheric plasma cannot provide the return current necessary to keep spacecraft charging under control. In this work, we perform Particle-In-Cell simulations to investigate the conditions under which a high-voltage electron beam can be emitted from a spacecraft and explore solutions that can mitigate spacecraft charging. The electron beam cannot simply be compensated for by an ion beam of equal current, because the Child-Langmuir space charge limit is violated under conditions of interest. On the other hand, releasing a high-density neutral contactor plasma prior and during beam emission is critical in aiding beam emission. We show that after an initial transient controlled by the size of the contactor cloud where the spacecraft potential rises, the spacecraft potential can settle into conditions that allow for electron beam emission. A physical explanation of this result in terms of ion emission into spherical geometry from the surface of the plasma cloud is presented, together with scaling laws of the peak spacecraft potential varying the ion mass and beam current. These results suggest that a strategy where the contactor plasma and the electron beam operate simultaneously might offer a pathway to perform beam experiments in the magnetosphere.

1. Introduction

High-power electron beams (with tens of keV energies and fraction of an Ampere currents) emitted from spacecraft in space have been used for many experimental purposes: plasma-wave excitation [*Raitt et al.*, 1995; *Huang et al.*, 1998], spacecraft-charging dynamics [*Myers et al.*, 1990], exploring magnetospheric morphology [*Nemzek et al.*, 1992], exploring distant electric fields [*Wilhelm et al.*, 1980], studying magnetospheric scattering processes [*Swanson et al.*, 1986], and atmospheric and ionospheric modification [*Neubert and Gilchrist*, 2004]. For a general review of uses of beam experiments in space, see *Winckler* [1992].

Electron beams from spacecraft have been propagated long distances through regions of the magnetosphere [*Hendrickson et al.*, 1975; *Hallinan et al.*, 1978; *Winckler*, 1980; *Pellat and Sagdeev*, 1980; *Zhulin et al.*, 1980; *Nemzek and Winckler*, 1991; *Lavergnat*, 1982; *Prech et al.*, 2002], but all of these beams were launched from spacecraft that were in the ionosphere, where the plasma is sufficiently dense to provide the return current needed to avoid the spacecraft charging to levels that prevent further beam emission.

SCATHA (also known as P78-2), on the other hand, was a rather unique experiment involving electron beams in the magnetosphere (at the geosynchronous orbit). Its objective was to study the plasma environment and its effect on spacecraft charging and to test techniques to discharge the spacecraft. One of these techniques was the ejection of an electron beam from an electron gun [*Cohen et al.*, 1980a], which operated in a regime of relatively low currents (10 μA to $\sim$ 10 mA) with energies up to 3 keV. Some SCATHA experiments investigated the simultaneous effect of the magnetospheric plasma and beam emission on the spacecraft potential. Experiments with low beam currents ($\sim$ 10 μA) confirmed that the return current from the plasma was sufficient to maintain the spacecraft potential below the beam energy and the electron beam could safely be emitted, while for larger beam currents ($\sim$ 100 μA) most of the beam electrons returned to the spacecraft [*Gussenhoven et al.*, 1980]. On the other hand, an experiment with higher current (6 mA of 3 keV electrons) caused the permanent failure of three different payloads and the interruption of telemetry for several seconds [*Cohen et al.*, 1980b].

There are some scientific drivers that demand the emission of a high-power electron beam from a spacecraft residing in the magnetosphere: one is to establish the exact magnetic connections between locations in the magnetosphere and locations in the ionosphere [*Borovsky et al.*, 2000; *MacDonald et al.*, 2012]. What holds back such experiments is the fear of deleterious spacecraft charging effects from the emission of a high-power electron beam in the low-density magnetosphere [*National Research Council*, 2012].

Emitting a high-power electron beam involves the removal of a substantial amount of charge from a spacecraft. For instance, to create an optical beamspot in the ionosphere that is visible from the ground (30 W of 3914-Å emission), an electron beam must have a power on the order of 10 kW. If the beam kinetic energy is 40 keV, then the beam current must be 0.25 A. If the beam fires for a duration of 1 s, then the beam removes 0.25 C of charge from the spacecraft. For reference, 1 C is a lightning-bolt worth of charge [cf. *Krehbiel et al.*, 1979; *Uman*, 1987, Table 7.2].

For spacecraft without electron-beam experiments, spacecraft charging in the magnetosphere has often been controlled with the use of a plasma contactor that emits a high-density cool plasma [e.g., *Olsen*, 1985; *Schmidt et al.*, 1995; *Comfort et al.*, 1998; *Torkar et al.*, 2001]. Here the charging is driven by photoelectron currents and the thermal fluxes of the ambient plasma particles [*DeForest*, 1972; *Whipple*, 1981]. These currents onto the spacecraft are on the order of tens of microampere. Electron beam experiments in the ionosphere have been successful with the use of plasma contactors [*Katz et al.*, 1994; *Prech et al.*, 1995], where the contactor plasma is thought to make an electrical connection of the spacecraft to the high-density cross-field-conductive ionosphere. For the fraction-of-an-ampere currents considered for beam experiments in the magnetosphere, the plasma contactor is not a proven concept.

An idea of the spacecraft charging problem for a high-power beam experiment in the magnetosphere can be obtained by the following estimate. Say a spacecraft emits a 0.25 A electron beam for 1 s, leaving 0.25 C of charge behind. If the spacecraft has operated a plasma contactor for 5 s before the electron beam was fired, then a plasma cloud with a diameter of about 5 km will be contacting the spacecraft, assuming the expansion speed of the cool contactor plasma was 1 km/s. If that 0.25 C of charge is transferred from the small spacecraft into the bigger plasma cloud, then the charge would be distributed over a spherical region of radius about 2.5 km. Using Coulomb's law $\phi = Q/4\pi\varepsilon_0 r$ for the potential ϕ of a sphere of radius r containing a charge Q (ε_0 is vacuum permittivity) yields a potential of the sphere of 9×10^5 V. For this space experiment to work, the residual charge from the electron beam must be rapidly moved far from the spacecraft, not just into the contactor cloud.

In an attempt to resolve the issues just described, in this paper we perform Particle-In-Cell (PIC) simulations to investigate the multiscale dynamical charging of a spacecraft due to the emission of a high-voltage electron beam and of a high-density contactor plasma, and to establish the physics principles that would allow beam experiments to operate in the magnetosphere. In particular, our main result is to highlight the critical role of the contactor plasma in controlling and mitigating the transient of the spacecraft potential, thus offering a viable pathway to perform beam experiments in the low-density magnetosphere.

Note that a beam-contactor experiment in the low-density magnetosphere will be operating in a new regime where computer simulations are needed to explore the physics of spacecraft charging. Experiments with electron beams and plasma contactors have been performed in the ionosphere, but owing to the high-density of the ambient plasma and to the substantial conductive nature of the ionospheric environment, these ionospheric experiments provide little insight as to the operation of an experiment in the magnetosphere and provide little validation of the simulations in the present paper.

The paper is organized as follows. In section 2 we introduce the collisionless, electrostatic, kinetic plasma model adopted in this study and describe the simulation parameters and setup for our investigations. In section 3 we present spacecraft charging simulations in various settings, including (i) the emission of an electron beam in vacuum, (ii) the emission of an electron beam and a compensating ion beam of equal current in vacuum, and (iii) the simultaneous emission of the electron beam and the contactor plasma. We show that emitting an ion beam is not an option for electron beam emission because the Child-Langmuir space charge limit is easily violated. On the other hand, the presence of the contactor plasma allows for ion emission on a much larger area and induces a transition from a planar geometry ion emission (strongly space charge limited) to a quasi-spherical geometry ion emission that is not space charge limited and facilitates beam

Table 1. Definitions of the Reference Quantities Used in the Normalization of the Model Equations[a]

Quantity	Symbol
Plasma density	$n_{\rm ref}$
Plasma temperature	$T_{\rm ref}$
Background magnetic field magnitude	B_0
Plasma Debye length	$\lambda_{\rm ref} = \sqrt{\frac{\varepsilon_0 T_{\rm ref}}{e^2 n_{\rm ref}}}$
Electron thermal velocity	$v_{th,\rm ref} = \sqrt{T_{\rm ref}/m_e}$
Electron plasma frequency	$\omega_{pe,\rm ref} = \sqrt{\frac{e^2 n_{\rm ref}}{\varepsilon_0 m_e}}$
Electron cyclotron frequency	$\omega_{ce,\rm ref} = eB_0/m_e$
Current density	$J_{\rm ref} = en_{\rm ref}v_{th,\rm ref}$
Current	$I_{\rm ref} = en_{\rm ref}v_{th,\rm ref}\lambda_{\rm ref}^2$

[a]Other parameters are elementary charge $e = 1.6 \times 10^{-19}$ C, electron mass $m_e = 9.1 \times 10^{-31}$ kg, and vacuum permittivity $\varepsilon_0 = 8.85 \times 10^{-12}$ F/m.

emission. Scaling laws of the spacecraft potential varying ion mass and beam current are also presented. The conclusions of our study are drawn in section 4.

2. Physics Model and Simulation Setup

We study the interaction of a collisionless plasma with a spherical spacecraft of radius $\rho_{\rm sp}$. The plasma is modeled kinetically; namely, it is described by a distribution function f_s (s labels the plasma species) that obeys the Vlasov equation

$$\frac{\partial f_s}{\partial t} + \mathbf{v} \cdot \nabla f_s + \frac{q_s}{m_s}\left(\mathbf{E} + \mathbf{v} \times \mathbf{B}_0\right) \cdot \nabla_v f_s = 0, \tag{1}$$

where q_s (m_s) is the particle charge (mass) for species s and ∇_v is the gradient operator in velocity space. The plasma moves under the action of the self-induced electric field $\mathbf{E}$, obtained from Poisson's equation

$$\nabla^2 \phi = -\frac{\sum_s q_s n_s}{\varepsilon_0} \tag{2}$$

(ϕ is the electrostatic potential, $\mathbf{E} = -\nabla\phi$, and n_s is the plasma density for species s) and of an external magnetic field $\mathbf{B}_0$. We introduce the following normalization: lengths are normalized to a reference Debye length $\lambda_{\rm ref} = \sqrt{\frac{\varepsilon_0 T_{\rm ref}}{e^2 n_{\rm ref}}}$ (where $n_{\rm ref}$ and $T_{\rm ref}$ are a reference density and temperature, $e = 1.6 \cdot 10^{-19}$ C is the elementary charge), $\hat{\mathbf{x}} = \mathbf{x}/\lambda_{\rm ref}$; velocity to the reference electron thermal velocity $v_{th,\rm ref} = \sqrt{T_{\rm ref}/m_e}$, $\hat{\mathbf{v}} = \mathbf{v}/v_{th,\rm ref}$; time to the reference electron plasma frequency $\omega_{pe,\rm ref} = \sqrt{\frac{e^2 n_{\rm ref}}{\varepsilon_0 m_e}}$, $\tau = \omega_{pe,\rm ref}t$; densities to a reference density, $\hat{n}_s = n_s/n_{\rm ref}$; temperatures to a reference temperature, $\hat{T}_s = T_s/T_{\rm ref}$; the electrostatic potential is normalized as $\psi = e\phi/T_{\rm ref}$; and the magnitude of the background magnetic field is normalized as $\hat{B}_0 = \frac{\omega_{ce,\rm ref}}{\omega_{pe,\rm ref}}$ with $\omega_{ce,\rm ref} = eB_0/m_e$ the electron cyclotron frequency. For ease of the notation, in the following we will drop hats with the understanding that we will always use normalized units. The normalization is summarized in Tables 1 and 2.

In this paper we study a system where a neutral plasma consisting of electrons and ions is emitted by the spacecraft and expands in vacuum. This plasma corresponds to the contactor plasma that is often used to control spacecraft charging, and in the following we will refer to it as the contactor plasma. After the contactor plasma has expanded for some time and created a plasma plume near the spacecraft, we emit an electron beam from the spacecraft and explore parametrically the conditions for which the beam can be emitted or returns to the spacecraft.

We note that in the present paper we do not consider the presence of a background plasma and its effect on the current loop on the spacecraft and the contactor. This is treated in [*Delzanno et al.*, 2015]. We also do not consider backscattered or secondary emission electrons that could follow from the absorption of primary (beam or contactor) electrons by the spacecraft. These effects are negligible when the spacecraft is positively charged by more than a few volts [*Hastings and Garrett*, 1996], which is the regime targeted by this paper. Furthermore, our results are relevant to eclipse conditions since we neglect photoemission. Finally, depending on the ionization efficiency, charge-exchange processes between contactor ions and neutrals could be important near the contactor injection point [*Katz et al.*, 1994]. Since we have neglected these effects, our results are relevant to a regime of high contactor ionization.

2.1. Simulation Setup
Numerically, the model described by equations (1) and (2) is solved with the PIC methodology [*Birdsall and Langdon*, 1985]. Specifically, we use a recently developed PIC code called Curvilinear PIC (CPIC) [*Delzanno*

Table 2. Summary of the Normalization Used in the Text Relative to the Quantities Defined in Table 1[a]

Quantity	Symbol	Normalization
Density species s	n_s	$\hat{n}_s = \frac{n_s}{n_{ref}}$
Temperature species s	T_s	$\hat{T}_s = \frac{T_s}{T_{ref}}$
Lengths	$\mathbf{x}$	$\hat{\mathbf{x}} = \frac{\mathbf{x}}{\lambda_{ref}}$
Spacecraft radius	ρ_{sp}	$\hat{\rho}_{sp} = \frac{\rho_{sp}}{\lambda_{ref}}$
Outer domain radius	ρ_2	$\hat{\rho}_2 = \frac{\rho_2}{\lambda_{ref}}$
Velocity	$\mathbf{v}$	$\hat{\mathbf{v}} = \frac{\mathbf{v}}{v_{th,ref}}$
Drift velocity species s	$\mathbf{V}_s$	$\hat{\mathbf{V}}_s = \frac{\mathbf{V}_s}{v_{th,ref}}$
Time	t	$\tau = \omega_{pe,ref} t$
Electrostatic potential	ϕ	$\psi = \frac{e\phi}{T_{ref}}$
Spacecraft potential	$\phi_{sp} = \phi(\rho_{sp})$	$\psi_{sp} = \frac{e\phi_{sp}}{T_{ref}}$
Magnetic field magnitude	B_0	$\hat{B}_0 = \frac{\omega_{ce,ref}}{\omega_{pe,ref}}$
Injected current density species s	J_s	$\hat{J}_s = \frac{J_s}{J_{ref}}$
Injection area	$\mathbb{A}$	$\hat{\mathbb{A}} = \frac{\mathbb{A}}{\lambda_{ref}^2}$
Injected current species s	$I_s = \mathbb{A} J_s$	$\hat{I}_s = \frac{I_s}{I_{ref}}$
Area enclosed by the spacecraft and density contour $n_s = \bar{n}$ for species s (Figure 1b)	$\mathcal{A}_{s,\bar{n}}$	$\hat{\mathcal{A}}_{s,\bar{n}} = \frac{\mathcal{A}_{s,\bar{n}}}{\lambda_{ref}^2}$

[a]The simulations are conducted in cylindrical (r, θ, z) geometry (assuming azimuthal symmetry for the electrostatic field) and $\rho = \sqrt{r^2 + z^2}$. In section 3 normalized quantities will always be used without hats to ease the notation.

et al., 2013]. CPIC couples the standard PIC algorithm with the ability to conform the computational grid to complex objects and has been used primarily for plasma-material interaction studies [*Delzanno et al.*, 2013; *Delzanno and Tang*, 2014].

We note that in the context of spacecraft-plasma interaction, several sophisticated codes have been developed across the globe: Nascap-2k [*Mandell et al.*, 2006] in the U.S., SPIS [*Roussel et al.*, 2008; *Matéo-Vélez et al.*, 2012] in Europe, and MUSCAT [*Muranaka et al.*, 2008] in Japan. Nascap-2k and SPIS solve Poisson's equation with iterative solvers (conjugate gradient or GMRES method) with some form of preconditiong, while MUSCAT uses the Fast Fourier Transform. For comparison, CPIC uses the (BlackBox) multigrid algorithm which is the only truly scalable Poisson solver (i.e., the computational time scales linearly with the number of unknowns). Nascap-2k uses nonuniform, structured computational meshes with adaptive mesh refinement to improve resolution where needed. SPIS uses unstructured meshes. Both options require a tracking algorithm to locate a particle in a cell which implies more computational time to move the particles. MUSCAT uses uniform (Cartesian) structured meshes, while CPIC uses nonuniform structured meshes. In both cases, particle tracking is trivial. Indeed, [*Delzanno et al.*, 2013] shows that the algorithm to move particles used in CPIC is more computationally efficient than a standard tracking algorithm. Furthermore, Nascap-2k is serial, SPIS features a parallelized mover, while both MUSCAT and CPIC are fully parallelized. Further details on the CPIC algorithm, together with some verification tests, can be found in *Delzanno et al.* [2013].

The simulations are conducted in cylindrical (r, θ, z) geometry, where azimuthal symmetry is assumed for the fields ($\partial/\partial\theta = 0$), while the particles retain three components of the velocity. The computational domain is enclosed by two concentric spheres of radius ρ_{sp} and ρ_2 (we define $\rho = \sqrt{r^2 + z^2}$) and is divided in $N_r \times N_z$ cells as described in *Delzanno et al.* [2013]. Thus, the spacecraft corresponds to the inner boundary of the simulation domain.

The external magnetic field is constant and directed along z. The contactor plasma is injected at $\rho = \rho_{sp}$ ($r \simeq 0$), antiparallel to the magnetic field. It is characterized by the density $n_s = n_p$, the drift velocity V_p, and the thermal velocity $v_{th,s} = \sqrt{T_s/m_s}$ (with $s = e, i$ labeling electrons and ions, respectively). Contactor electrons are injected in the system according to a half-width Maxwellian distribution at rest, since $v_{th,e} \gg V_p$. Contactor ions, on the other hand, are cold ($v_{th,i} \ll V_p$) and are injected in the contactor plasma as a beam plus a small
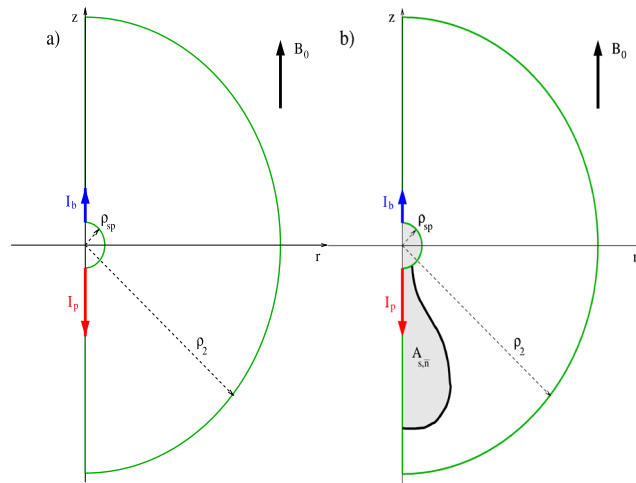
Figure 1. (a) Cartoon of the simulation setup. (b) Schematics of $\mathcal{A}_{s,\bar{n}}$. The black thick line represents the density contour corresponding to $n_s = \bar{n}$. $\mathcal{A}_{s,\bar{n}}$ is the area enclosed by the spacecraft and the density contour $n_s = \bar{n}$, and is used for diagnostic purposes in section 3.

thermal spread. The electron beam (labeled with $s = b$) is injected at $\rho = \rho_{sp}$ ($r \simeq 0$) parallel to the magnetic field, with density n_b, drift velocity V_b, and no thermal spread. The injection area $\mathbb{A}$ on the spacecraft is the same for both the contactor plasma and the beam, and is expressed in terms of an injection angle θ^*:

$$\mathbb{A} = 2\pi \rho_{sp}^2 (1 - \cos \theta^*). \qquad (3)$$

The number of particles injected from the spacecraft surface per species at each time step of the simulation is 400; self-consistent charging effects will dictate how many leave the vicinity of the spacecraft and how many return to it. A cartoon of the simulation setup is presented in Figure 1a.

The particles injected in the system move under the action of the self-consistent electric field and external magnetic field. Particles that hit the spacecraft are removed from the simulation, and their charge is accumulated onto the spacecraft. This translates into a boundary condition on the electric field (via Gauss' law for a perfectly conducting body) at the inner boundary of the simulation domain. Particles can also exit the system at the outer boundary ρ_2, implying that the net charge in the simulation domain including the spacecraft is not necessarily zero. At the outer domain, we use a Dirichlet (i.e., conducting) boundary condition on the electrostatic potential: $\psi(\rho_2) = 0$.

Our reference simulation parameters are as follows:

1. Background magnetic field magnitude: $B_0 = 3 \times 10^{-3}$.
2. Geometrical parameters: $\rho_{sp} = 1$, $\rho_2 = 50$, $\theta^* = 14°$, $\mathbb{A} = 0.187$.
3. Contactor plasma parameters: $n_p = 100$, $V_p = 0.01$, $T_e = 0.01$, $T_i = 0.01$, $\frac{m_i}{m_e} = 1836$.

This gives a contactor current density $J_p = n_p V_p = 1$ and a contactor current $I_p = I_i = \mathbb{A} J_p = 0.187$. Initially, we perform simulations of the expansion of the contactor plasma prior to beam emission to obtain configurations characterized by a different size of the contactor cloud. Specifically, we consider three contactor configurations obtained at times $\tau = 200$, 600, and 1000, and label them as 1, 2, and 3, respectively. These configurations are later used as initial conditions for studies of beam emission (where the contactor plasma continues to be injected). Our beam reference parameters are listed in Table 3. For cases $A_1 - A_3$ and $B_1 - B_3$, the contactor current density is greater than the beam current density $J_b = n_b V_b = 0.5$. Note that we also study cases where we do not actually simulate the electron beam but only account for its effect by removing the beam charge $\mathbb{A} J_b \Delta\tau$ at every time step $\Delta\tau$. We label these cases as $C_1 - C_3$ in Table 3, and J_b will be specified separately for each case.

The simulations are conducted on a grid with $N_r = 4096$ and $N_z = 1024$ and ran on 256 processors of the Mapache cluster at the Los Alamos National Laboratory.

We note that the reference parameters just discussed are rescaled (but keeping ratios of relevant quantities in the right range) relative to realistic values for a contactor plasma/beam system, as normally done to keep the

Table 3. Electron Beam Parameters for the Simulations of Section 3

Case	n_b	V_b	J_b	$\Delta\tau$	Initial Contactor Configuration at Time
A_1					$\tau = 200$
A_2	0.5	1	0.5	0.01	$\tau = 600$
A_3					$\tau = 1000$
B_1					$\tau = 200$
B_2	0.25	2	0.5	0.005	$\tau = 600$
B_3					$\tau = 1000$
C_1					$\tau = 200$
C_2	Beam charge $\mathbb{A}J_b\Delta\tau$ removed from spacecraft without simulating the beam		to be specified	0.02	$\tau = 600$
C_3					$\tau = 1000$

cost of simulations manageable. For instance, assuming $n_{ref} = 10^4$ cm^{-3} and $T_{ref} = 1$ keV ($\lambda_{ref} = 2.3$ m) gives a contactor peak density at injection $n_p = 10^6$ cm^{-3}, lower than typical values. This would be consistent with the inner boundary of our simulation domain ($= \lambda_{ref} = 2.3$ m since $\rho_{sp} = 1$) corresponding not to the actual physical boundary of the spacecraft but rather to the boundary where the contactor density has dropped to the level considered (one can estimate that this happens a few meters from the spacecraft). Assuming a background magnetic field of 100 nT (typical of geosynchronous orbit) leads to $B_0 = 3 \times 10^{-3}$ considered in this study. Furthermore, for $T_{ref} = 1$ keV, the contactor temperature is $T_e = T_i = 10$ eV and its drift velocity is $V_p = 100$ km/s with $m_i/m_e = 1836$. This choice is reasonable for the electron temperature and drift velocity relative to a high-voltage contactor that operates with Helium, but typically, the ions are at least one order of magnitude colder. Also, a more typical Xenon contactor would have drift velocities of the order of ~ 10 km/s. Our rescaled choice in this case increases the ion Debye length at injection (which needs to be resolved in a standard PIC code) but remains in the relevant range $V_p \gg v_{th,i}$ and $V_p \ll v_{th,e}$. Furthermore, while the majority of the runs is conducted with the proton mass, we will also perform some studies varying the ion mass in order to identify the relevant scaling laws. The point of the present paper is to demonstrate the physical principles that will enable beam experiments to operate in the low-density magnetosphere. Simulations with the exact engineering parameters of an actual space experiment are left for the future.

One more comment is in order with regard to using electrostatic simulations for these studies. For a space-experiment beam current of the order of 0.1 A, an application of the Biot-Savart law indicates that a perpendicular distance of ~ 1–2 m from injection the induced magnetic field is already 5–10 times smaller than the background field and should therefore be negligible. Furthermore, the high contactor density implies that close to injection the plasma $\beta = 2\mu_0 n_p T_p/B_0^2 \gg 1$ (μ_0 is vacuum permeability) with the potential for electromagnetic instabilities. Our preliminary simulation results carried out with a two-fluid electromagnetic code indicate that instabilities do not occur for regimes $\omega_{pe,ref}/\omega_{ce,ref} \gg 1$ as considered here.

Finally, although in this paper we do not focus on the effect of the background plasma, in an attempt to provide some comparison with actual data, we have performed some simulations relevant to SCATHA experiments (not shown). Specifically, we have reproduced simulation 1 of Table 1 of *Rubin et al.* [1980], where a beam with energy 0.3 keV and current 100 μA was emitted by SCATHA with background plasma conditions typical of 30 March 1979 (single Maxwellian fit). In agreement with the work presented in *Rubin et al.* [1980], our simulation shows that the spacecraft potential saturates above the gun energy and most of the beam returns to the spacecraft (cf. section 3.1). In our simulation the maximum potential on the spacecraft is 326 V, in good agreement with 338 V from *Rubin et al.* [1980]. Moreover, a complete study of the effects of the background plasma is presented in *Delzanno et al.* [2015], where it is shown that the results obtained in this paper for the vacuum case are a good approximation to the low-density magnetospheric conditions typical of geosynchronous orbit.

3. Results

In this section we perform PIC simulations to investigate electron beam emission from the spacecraft and the related problem of spacecraft charging in various settings. These include electron beam emission in vacuum,
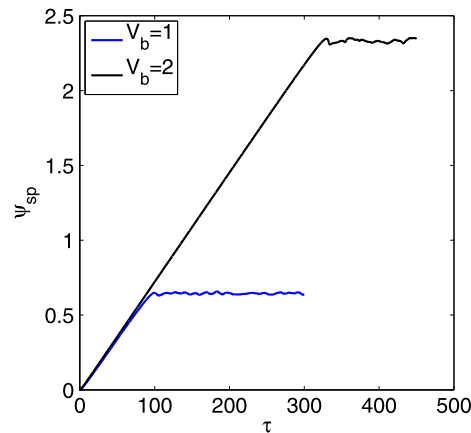
Figure 2. Simulations of electron beam emission without contactor plasma: spacecraft potential as a function of time.

the attempted emission of an electron and a compensating ion beam of equal current in vacuum, and the emission of the electron beam together with the contactor plasma.

Since our interest is to identify conditions that allow beam emission for longer times, we monitor the spacecraft potential in all simulations: when the spacecraft potential is (well) below the beam kinetic energy, the beam can be emitted. If the opposite is true, the spacecraft charging is too strong and the beam returns to the spacecraft.

We also define certain diagnostic quantities that are useful for the interpretation of the data. Specifically, we define the parameter $\mathcal{A}_{s,n}$ equal to the area enclosed by the spacecraft surface plus the density contour level corresponding to $n_s = n$ for each plasma species s (see Figure 1b). Similarly, for each density contour we define an equivalent (spherical) radius $\mathcal{R}_{s,n}$ as

$$\mathcal{A}_{s,n} = \frac{\pi}{2}\left(\mathcal{R}_{s,n}\right)^2 . \qquad (4)$$

3.1. Simulations of Electron Beam Emission Without Plasma Contactor

We have performed some simulations considering only the electron beam emission from the spacecraft, in order to set the reference for the simulations combining beam emission and the contactor plasma. As the electron beam is emitted from the spacecraft into vacuum, the spacecraft becomes positively charged and its potential rises in time. From a steady state point of view, beam emission can occur only until the spacecraft electrostatic potential is equal to the kinetic energy of a beam electron. In normalized units, this corresponds to

$$\psi_{\mathrm{sp}} = \psi\left(\rho_{\mathrm{sp}}\right) = \frac{V_b^2}{2}. \qquad (5)$$

Using the spacecraft charge versus potential relation, $Q_{\mathrm{sp}} = C_{\mathrm{sp}}\psi_{\mathrm{sp}}$ (where $C_{\mathrm{sp}} = 4\pi\rho_{\mathrm{sp}}$ is the vacuum capacitance of a spherical body, and Q_{sp} is the spacecraft charge) and the fact that

$$Q_{\mathrm{sp}} = \mathbb{A}J_b\tau, \qquad (6)$$

expression (5) can be used to estimate the critical time when the beam returns to the spacecraft. After some simple algebra, it follows that

$$\tau_r = \frac{1}{\rho_{\mathrm{sp}}\left(1 - \cos\theta^*\right)}\frac{V_b^2}{J_b}, \qquad (7)$$

where we have used expression (3). Fixing the spacecraft geometry (ρ_{sp}) and the injection properties (θ^*, J_b), the beam return time scales as $\tau_r \propto V_b^2$. Clearly, if one can manage a higher spacecraft potential, a higher beam velocity is more favorable for beam emission. It also helps in terms of beam focusing, since higher velocities correspond to lower densities and therefore lower beam space charge.

Figure 2 shows the time dependent spacecraft potential obtained for $V_b = 1$ and $V_b = 2$, with $J_b = 0.5$. As expected, the spacecraft potential rises linearly in time until $\psi_{\mathrm{sp}} \sim V_b^2/2$ where the curves bend and saturate at $\psi_{\mathrm{sp}} \simeq 0.65$ for $V_b = 1$ and $\psi_{\mathrm{sp}} \simeq 2.3$ for $V_b = 2$. The observed time corresponding to $\psi_{\mathrm{sp}} = V_b^2/2$ is $\tau_r \simeq 73$ for $V_b = 1$ and $\tau_r \simeq 276$ for $V_b = 2$; these simulation times are in reasonable agreement with the predicted times $\tau_r\left(V_b = 1\right) \simeq 67$ and $\tau_r\left(V_b = 2\right) \simeq 267$ from expression (7). Figure 3 shows snapshots of the electron density at different times for the simulation with $V_b = 2$: at $\tau = 30$ (left) the beam is emitted by the spacecraft; at $\tau = 270$ (center) the beam slows down and opens up as the spacecraft electrostatic potential is becoming comparable to the beam energy; at $\tau = 333$ (right) the beam is electrostatically pulled back to the spacecraft.

For $n_{\mathrm{ref}} = 10^4$ cm^{-3} and $T_{\mathrm{ref}} = 1$ keV, during $\tau = 300$ the beam would cover only 1.4 km before returning to the spacecraft, implying that it would be impossible to map magnetic field lines over vast regions of space without some strategy that allows beam emission for longer times.
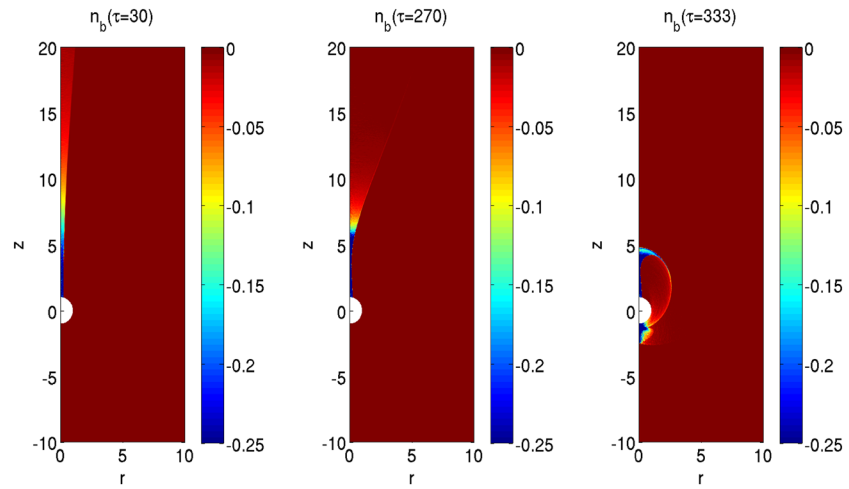
Figure 3. Simulations of electron beam emission without contactor plasma for $V_b = 2$: beam density (saturated at $n_b = -0.25$) at times (left) $\tau = 30$, (center) $\tau = 270$, and (right) $\tau = 333$.

3.2. Balancing the Electron Beam With an Ion Beam

When trying to emit an electron beam from a spacecraft without encountering the spacecraft charging problems discussed in section 3.1, an obvious idea is to balance the electron beam with an ion beam of equal current. While this is reasonable in theory, in practice it is notoriously difficult to draw a large ion current because of space charge effects, a result that dates back to the pioneering work of Child [*Child*, 1911]. In order to see this, we have performed a PIC simulation where at time $\tau = 0$ an ion beam with current density $J_i = 0.5$ (characterized by $n_i = 50$ and $V_i = 0.01$) and current $I_i = 0.093$ is injected anti-parallel to the background magnetic field, in addition to the electron beam (with $n_b = 0.5$ and $V_b = 1$) discussed in section 3.1. A straightforward application of the planar Child-Langmuir law [*Child*, 1911; *Langmuir and Blodgett*, 1924; *Lieberman and Lichtenberg*, 2005] gives the maximum ion current J_{CL}^{planar} that can be drawn before space charge effects become dominant. We solve Poisson's equation in planar geometry for ions emitted at the boundary $x = \rho_{sp}$ with velocity $V_i = V_p$ and whose steady state density is obtained by using the conservation of mass and energy:

$$\frac{d^2\psi}{dx^2} = -\frac{J_i}{V_i}\frac{1}{\sqrt{1+\frac{\psi_{sp}-\psi}{\varepsilon}}}, \tag{8}$$

with $\varepsilon = \frac{1}{2}\frac{m_i}{m_e}V_i^2$ and boundary conditions $\psi(\rho_{sp}) = \psi_{sp}$ and $\psi(\rho_2) = 0$. The additional constraint $\frac{d\psi}{dx}\big|_{x=\rho_{sp}} = 0$ is used to obtain J_{CL}^{planar}:

$$J_{CL}^{planar} = \frac{4}{9}\frac{\varepsilon V_i}{(\rho_2-\rho_{sp})^2}\left(\sqrt{1+\frac{\psi_{sp}}{\varepsilon}}-1\right)\left(\sqrt{1+\frac{\psi_{sp}}{\varepsilon}}+2\right)^2. \tag{9}$$

If one assumes $\psi_{sp} = V_b^2/2$ ($V_b = 1$ and $m_i/m_e = 1836$), it is straightforward to see that $J_{CL}^{planar} \simeq 5.4 \times 10^{-6} \ll J_i$ and the ion beam cannot really be emitted. (In practice the situation is less dramatic since the Child-Langmuir current for a finite-width beam is larger than that given by equation (9) [*Lau*, 2001] but is still not enough to allow ion beam emission.) Essentially, the ions create a virtual anode in front of the injection aperture (i.e., the ion front is at higher potential than the spacecraft) that returns most of the ions to the spacecraft and lets only a small current escape [*Wang and Lai*, 1997]. The virtual anode can be clearly seen in Figure 4 (it corresponds to the area enclosed by the contour $\psi = \psi_{sp} = 0.62$) showing the electrostatic potential
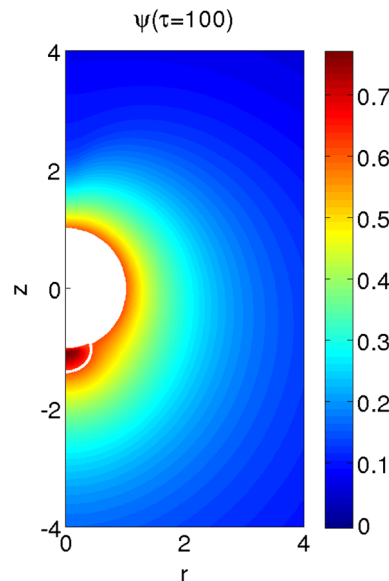

Figure 4. Balancing the electron beam with an ion beam: electrostatic potential near the spacecraft at time $\tau = 100$. The contour $\psi = \psi_{sp} = 0.62$ is plotted with a white line and encloses the area of the virtual anode.
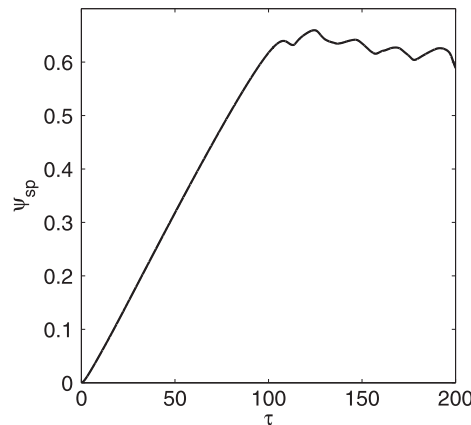
Figure 5. Balancing the electron beam with an ion beam: spacecraft potential as a function of time.

near the spacecraft at time $\tau = 100$ from the PIC simulation. Thus, it is not surprising that the dynamics of the spacecraft potential resembles that of Figure 2, as can be seen in Figure 5, and that the electron beam can no longer be emitted for $\tau \gtrsim 100$.

It is interesting to repeat the same analysis of the Child-Langmuir law performed above in spherical geometry [*Langmuir and Blodgett*, 1924]. This amounts to solving Poisson's equation

$$\frac{1}{\rho^2}\frac{d}{d\rho}\left(\rho^2\frac{d\psi}{d\rho}\right) = -\frac{\rho_{sp}^2}{\rho^2}\frac{J_i}{V_i}\frac{1}{\sqrt{1+\frac{\psi_{sp}-\psi}{\varepsilon}}} \qquad (10)$$

with the same boundary conditions as before. Unlike the planar case, the solution cannot be found analytically. We have solved equation (10) numerically and for $\psi_{sp} = V_b^2/2$ and $V_b = 1$ we f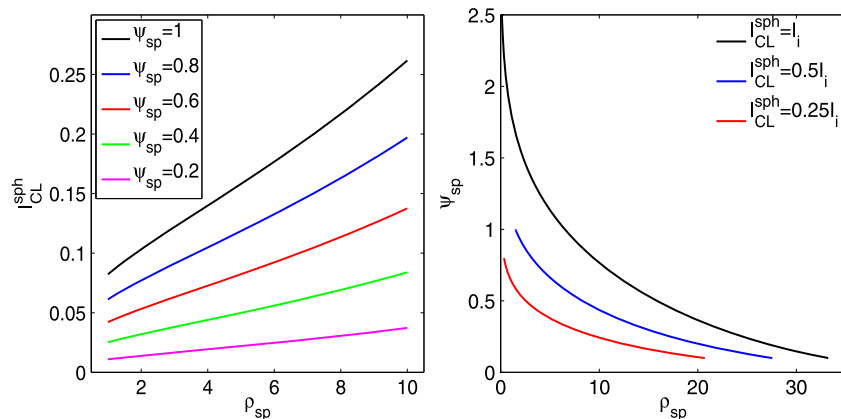ind $J_{CL}^{sph} = 2.7 \times 10^{-3}$ and $I_{CL}^{sph} = 4\pi\rho_{sp}^2 J_{CL}^{sph} = 0.033$. J_{CL}^{sph} is almost 3 orders of magnitude larger than J_{CL}^{planar}, implying that it is much easier to draw an ion current in spherical geometry. In addition, injecting over a larger area allows a bigger current, as can be seen in Figure 6 (left) where I_{CL}^{sph} is plotted for different values of ρ_{sp} and ψ_{sp} (all the other parameters are unchanged). A least squares fit of the data of Figure 6 (left) indicates that $I_{CL}^{sph} \propto \rho_{sp}^{0.52-0.56}$. Figure 6 (right) shows the spacecraft potential versus the spacecraft radius obtained by the spherical Child-Langmuir law where we impose the additional constraint that $I_{CL}^{sph} = \gamma I_i$ with $\gamma = 0.25, 0.5, 1$ and $I_i = 0.187$ (i.e., the value of the contactor current used in this study).

While the engineering of a spacecraft into a spherical ion emitter is impractical, the importance of this result cannot be underestimated: if the ions could somehow be emitted over a larger spherical area, electron beam emission would be facilitated. In the next section we will show that the contactor plasma could indeed be used for this purpose.

3.3. Simulations of Beam and Contactor Emission
3.3.1. Characterization of the Contactor Plasma Cloud Prior to Beam Emission

In this section we investigate the expansion of the contactor plasma emitted by the spacecraft before firing the electron beam. Figure 7 shows the spacecraft potential as a function of time. It also marks (with dashed lines) the times corresponding to three contactor plasma configurations that will be used in section 3.3.2 as initial conditions to study beam emission. Since for our parameters the injected contactor electron current is larger than the contactor ion current, $I_e/I_i \simeq 4$, the spacecraft charges slightly positively and creates a sheath

Figure 6. Balancing the electron beam with an ion beam: (left) Child-Langmuir ion current I_{CL}^{sph} versus spacecraft radius for different values of ψ_{sp}, obtained in spherical geometry from the calculation discussed in section 3.2. (right) The spacecraft potential versus radius with the additional constraint that $I_{CL}^{sph} = \gamma I_i$ ($\gamma = 0.25, 0.5, 1$ and $I_i = 0.187$). The ion mass ratio is $\frac{m_i}{m_e} = 1836$.
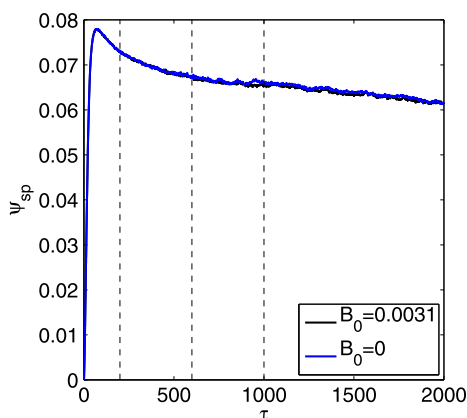
Figure 7. Characterization of the contactor plasma prior to beam emission: spacecraft potential as a function of time.

that turns some of the emitted contactor electrons back onto the spacecraft to reduce the electron current to $I_e \sim I_i$. Initially, the spacecraft potential rises sharply, peaking at $\psi_{sp}(\tau \simeq 70) \simeq 0.078$ and then slowly decaying. The contactor electron thermal velocity is much larger than the drift velocity while the opposite is true for the contactor ions. Therefore, the electrons outrun the ions at the beginning of the dynamics and tend to move quite isotropically due to the electric field near the spacecraft. For this reason and since the spacecraft is positively charged, some electrons move around the spacecraft and some are re-collected: within $\tau = 40$ the spacecraft is surrounded by a low-density electron cloud that extends well beyond the ion cloud. This can be seen in Figures 8a–8c, which shows contours of the electron density for $n_e = 10^2$, 10, 1, 10^{-1}, 10^{-2} corresponding to $\tau = 4$ (a), $\tau = 12$ (b) and $\tau = 40$ (c). We note that the lowest electron density contour is very diffuse and not well resolved, as one can distinguish the individual particles. For comparison, the ion density at $\tau = 40$ is also plotted in Figure 8d. Figure 9 shows the ion density at time $\tau = 200$, $\tau = 600$ and $\tau = 1000$ and the electron density at $\tau = 1000$. One can see that the plasma expansion is mostly quasi-neutral, with density contours overlapping almost perfectly down to
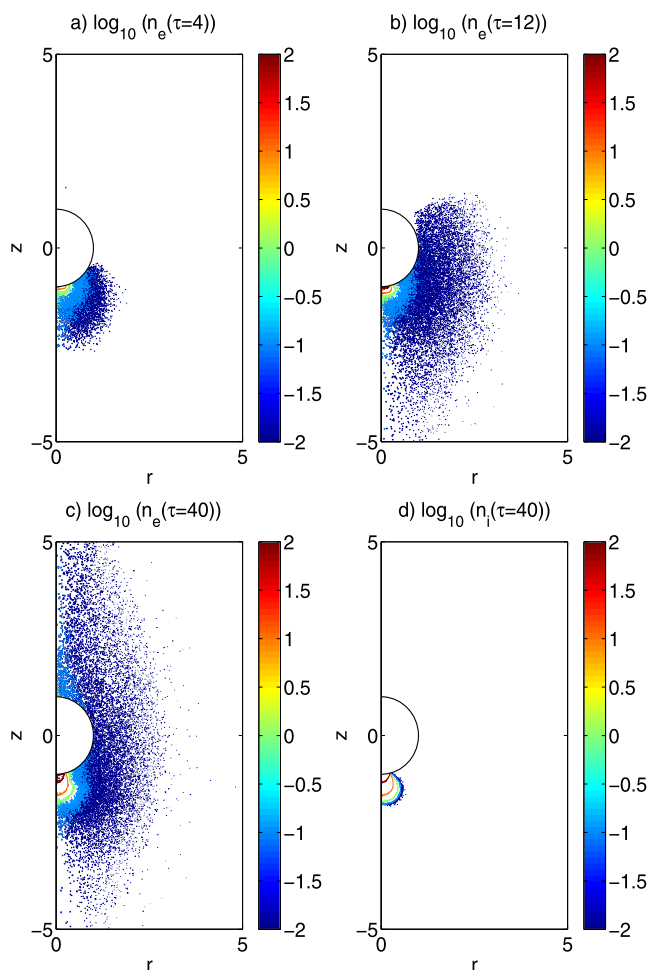

Figure 8. Characterization of the contactor plasma prior to beam emission: electron density at (a) $\tau = 4$, (b) $\tau = 12$, (c) $\tau = 40$, and ion density at (d) $\tau = 40$.
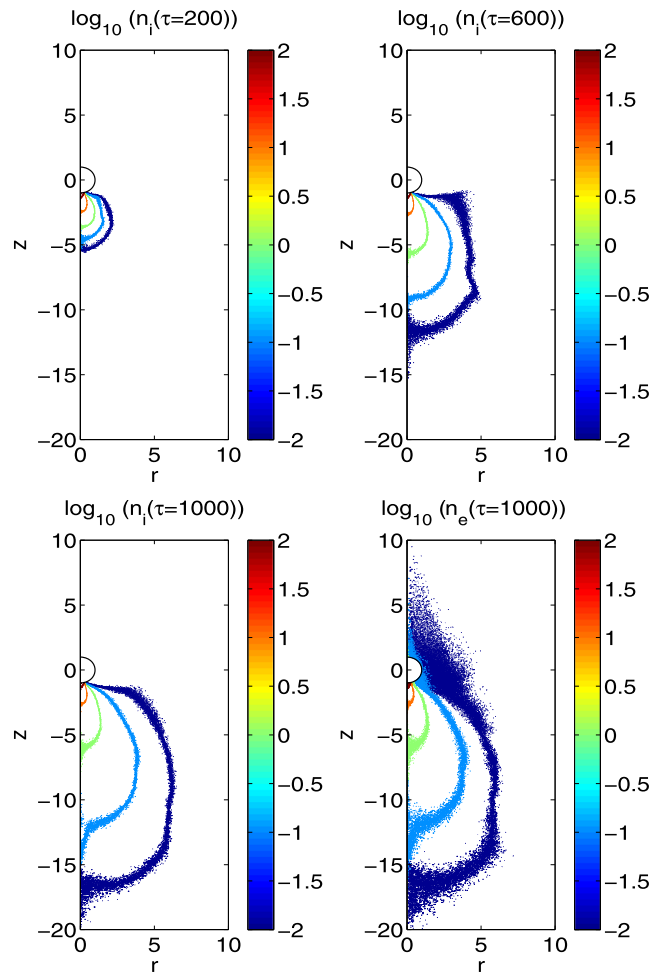
Figure 9. Characterization of the contactor plasma prior to beam emission: ion density at $\tau = 200$, $\tau = 600$, and $\tau = 1000$, and electron density at $\tau = 1000$.

$n \sim 0.1$. This is less true for lower densities, particularly with regard to the low electron density cloud that forms on top of the spacecraft where there are no ions.
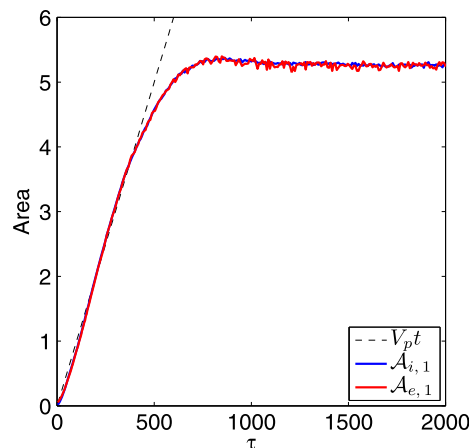

Figure 10. Characterization of the contactor plasma prior to beam emission: $\mathcal{A}_{s,1}$ as a function of time.

Figure 10 shows $\mathcal{A}_{s,1}$ as a function of time. By definition $\mathcal{A}_{s,1}$ encloses the region where $n_s \geq 1$ and is representative of the high density part of the contactor cloud ($n_s/n_p \geq 1\%$, where n_p is the density of the contactor plasma at the point where it is emitted). After the initial phase where the electrons outrun the ions (hence $\mathcal{A}_{e,1} > \mathcal{A}_{i,1}$), the two areas become approximately equal, consistent with quasi-neutrality as discussed above. From Figure 10 one can see that the initial expansion of the quasi-neutral plasma is dictated by the ions and is roughly characterized by the curve $V_p t$ (a least squares fit of $\mathcal{A}_{i,1}$ between $\tau = 100$ and $\tau = 300$ gives $\mathcal{A}_{i,1} \propto t^{1.17}$), consistent with an expansion that is stretched along the injection axis.

We have also performed some simulations setting the background magnetic field to zero in order to investigate its role in the expansion. For our parameters, the electron
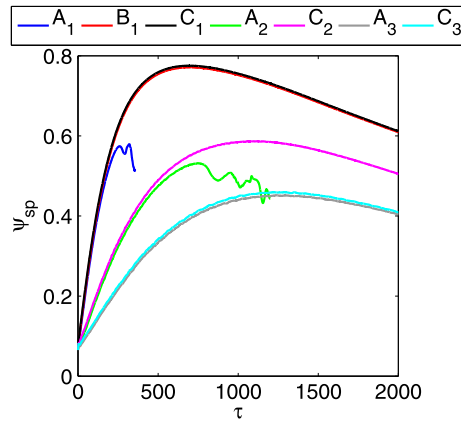
Figure 11. Simulations of contactor and beam emission: spacecraft potential for various beam velocities and initial contactor configurations, following the classification discussed in Table 3. Other parameters are $J_b = 0.5$ and $\frac{m_i}{m_e} = 1836$.

gyroradius is $r_e \simeq 32$, much larger than the radial characteristic scale of the plasma cloud for the simulations that we performed. Consistently, we have not found a significant impact of the background field on the spacecraft potential (Figure 7) or on the plasma densities.

3.3.2. Simulations of the Contactor Plasma With Beam Emission

In this section we analyze simulations in which the electron beam is turned on after the contactor plasma has been injected for some time and a contactor cloud has already formed. The contactor plasma continues to be injected during these simulations. Figure 11 shows the spacecraft potential for three different initial configurations of the contactor plasma and for different values of the beam velocity (all with $J_b = 0.5$), following the classification that was introduced in Table 3. Let us consider the curves for cases $A_1 - C_1$, where the initial contactor plasma corresponds to $\tau = 200$ in Figure 9. For case A_1 ($V_b = 1$) the spacecraft potential rises to a value that exceeds the beam kinetic energy and the beam returns to the spacecraft after $\tau \sim 260$. Compared to Figure 2 where the beam returns to the spacecraft after $\tau \sim 100$, the contactor allows for longer beam emission but still cannot prevent the beam return. For case B_1 ($V_b = 2$), on the other hand, the spacecraft potential rises, reaches its maximum ψ_{sp}^{max} ($\tau \simeq 700$) $\simeq 0.78$ and then decreases. ψ_{sp}^{max} is much lower than the beam kinetic energy and the beam never returns to the spacecraft. Case C_1 (equivalent to $V_b \longrightarrow \infty$, where we simply remove the beam charge from the spacecraft but do not simulate the beam) is surprisingly close to B_1, indicating that the functional dependence of the spacecraft potential on the beam velocity saturates for $V_b \gtrsim 2$. The larger contactor cloud cases A_2, C_2 and cases A_3, C_3 follow similar trends relative to A_1-C_1, with the most important differences being: (1) the spacecraft potential peaks at lower values with larger contactor clouds, and (2) while for A_2 the beam returns to the spacecraft after $\tau \sim 750$, for A_3 (with the largest contactor cloud) it never does since ψ_{sp}^{max} is always lower than the beam kinetic energy.

When the electron beam is initially turned on, the spacecraft potential has a transient sharp rise (with $Q_{sp} \sim I_b\tau$ for $\tau \lesssim 4$), then the contactor and its currents readjust and the subsequent rise of ψ_{sp} (which is more clearly visible in Figure 11) is more moderate. In fact, an analysis of the contactor currents from the spacecraft for the cases in Figure 11 reveals that in the initial short transient the contactor electron current I_e readjusts to $I_e \simeq I_i - I_b = I_i/2$ such that $I_e + I_b$ is slightly larger than I_i. The (initial) slope of this subsequent part of the rise of the spacecraft potential can be estimated by noting that beam emission perturbs the charge over an area enclosing the spacecraft and the ion contactor cloud. The same capacitance-type argument used in section 3.1 can be used here, leading to

$$\psi_{sp} = \frac{I_b}{C}\tau, \tag{11}$$

where now the capacitance C is calculated on the area of the spacecraft and the contactor cloud and we have assumed it at $\psi \simeq \psi_{sp}$. In order to cast things in more concrete terms, we have computed the area $\mathcal{A}_{i, 10^{-6}}$ of the $n_i = 10^{-6}$ contour and its equivalent radius $\mathcal{R}_{i, 10^{-6}}$ for the three initial configurations corresponding to C_1-C_3 to obtain an equivalent capacitance $C = 4\pi\mathcal{R}_{i, 10^{-6}}$ that could be used to compute I_b/C. The results of the comparison of this method with a numerical evaluation of $d\psi_{sp}/d\tau$ are shown in Table 4, indicating good agreement between the two (the relative error is less than 15%).

In order to gain more insight on the system dynamics, we look in Figure 12 at the evolution of the contactor cloud electron density for simulation B_1. Qualitatively the contactor cloud continues to expand similarly to the
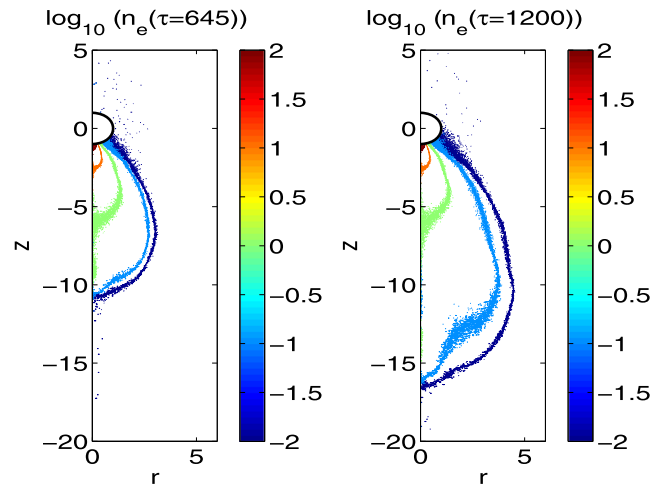
Table 4. Calculation of the Positive Slope of ψ_{sp} in Figure 11, $J_b = 0.5$

Simulation	$\mathcal{A}_{i, 10^{-6}}$	I_b/C	$\left.\dfrac{d\psi_{sp}}{d\tau}\right|_{num}$
C_1	10.6	2.9×10^{-3}	3.2×10^{-3}
C_2	98.1	9.4×10^{-4}	1.1×10^{-3}
C_3	294.2	5.4×10^{-4}	6.1×10^{-4}

Figure 12. Simulations of contactor and beam emission: contactor electron density at (left) $\tau = 645$ and (right) $\tau = 1200$ for case B_1.

case without beam emission discussed in section 3.3.1. It is characterized by a quasi-neutral, high-density inner portion that reaches a steady state, and a non-neutral, low-density outer portion that keeps expanding. This can be seen clearly in Figure 12, where the contactor electron density contours (with the same format of Figure 8) at two different times are compared. We also look at the electrostatic potential in the simulation domain. Figure 13 shows plots of the electrostatic potential on the negative z axis, $\psi(r = 0, z < 0)$, at various times. In general one can see that the potential is mostly monotonic, with a moderate gradient near the spacecraft followed by a vacuum-like ($\sim \rho^{-1}$) solution. In Figure 13 we have superimposed three curves that correspond to the instantaneous positions z^* that three electrons injected on the z axis with initial velocity $v_z = -v_{th,e}$ (i.e., $\Delta\psi(\tau) = \psi_{sp}(\tau) - \psi(0, z^*, \tau) = \frac{1}{2}\left(v_{th,e}\right)^2$), $v_z = -2v_{th,e}$ and $v_z = -3v_{th,e}$ would reach. Given that the contactor electrons are injected with a Maxwellian distribution, these three velocities are representative of most the injected electrons, including those in the tail of the distribution. One can see from Figure 13 that the curve $\Delta\psi = \frac{1}{2}\left(v_{th,e}\right)^2$ remains mostly constant at $z^* \sim -1.9$, while the curve $\Delta\psi = \frac{1}{2}\left(3v_{th,e}\right)^2$ is increasing monotonically and more so at later times. The curve $\Delta\psi = \frac{1}{2}\left(2v_{th,e}\right)^2$ exhibits an initial phase of growth but tends to saturate as time progresses. Interestingly, the curve $\Delta\psi = \frac{1}{2}\left(3v_{th,e}\right)^2$ follows quite well the transition of the potential to its vacuum solution. From Figures 12 and 13, it is clear that the bulk of the electron population with velocity $v \lesssim 2v_{th,e}$ gives rise to the quasi-neutral part of the contactor plasma, while the tail of the electron velocity distribution controls the expansion of the electron contactor cloud and is responsible for the contactor electron current I_e.
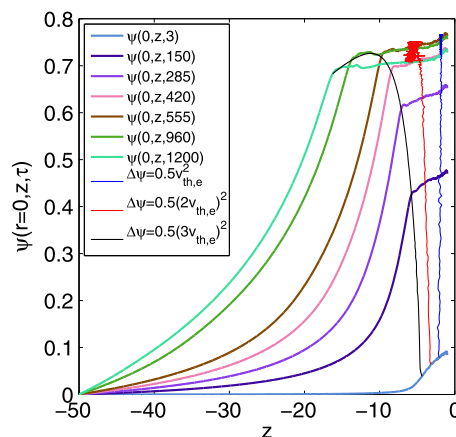
The nonmonotonic behavior in Figure 11 remains to be discussed. We have already noted that the rise of the spacecraft potential is due to the fact that $I_e + I_b \gtrsim I_i$. Not surprisingly, the decreasing phase is in the opposite limit, $I_e + I_b \lesssim I_i$. Our interpretation of this result is in terms of the Child-Langmuir law in spherical geometry discussed in section 3.2. Initially, the equivalent radius of the quasi-neutral contactor plasma (i.e., the region where the net (positive) current is $I = I_i - I_e$) is below the radius where the Child-Langmuir current is equal to $I_b = 0.093$ (Figure 6 (left), where I plays the role of I_{CL}^{sph} and the equivalent radius of the quasi-neutral cloud plays the role of ρ_{sp}). The spacecraft potential rises since $I < I_b$, the quasi-neutral contactor expands and its equivalent radius grows. From Figure 6 (left),

Figure 13. Simulations of contactor and beam emission: potential $\psi(r = 0, z)$ at various times for case B_1. The curves corresponding to $\Delta\psi(\tau) = \psi_{sp}(\tau) - \psi(0, z^*, \tau) = \frac{1}{2}\left(v_{th,e}\right)^2$, $\Delta\psi(\tau) = \frac{1}{2}\left(2v_{th,e}\right)^2$ and $\Delta\psi(\tau) = \frac{1}{2}\left(3v_{th,e}\right)^2$ are also superimposed.
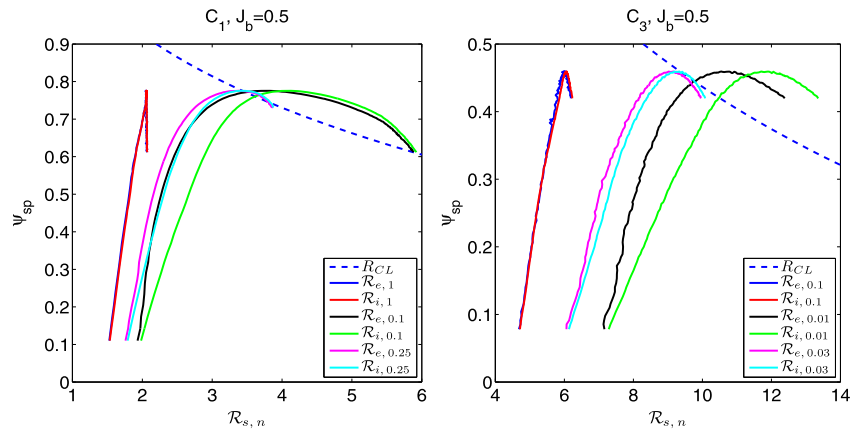
Figure 14. Simulations of contactor and beam emission: spacecraft potential versus equivalent radii $\mathcal{R}_{s,n}$ for cases (left) C_1 and (right) C_3. The radius obtained by the Child-Langmuir law in spherical geometry when $I_{CL}^{sph} = I_b = 0.093$ (from Figure 6, right) is plotted with a dashed line.

larger equivalent radii and larger spacecraft potential correspond to larger net ion current I off the cloud surface, namely the imbalance between I and I_b is reduced and the spacecraft potential grows at a slower pace. When the equivalent radius of the quasi-neutral cloud reaches the conditions such that $I = I_b$, the spacecraft potential peaks. If the quasi-neutral expansion continues, then $I > I_b$ and the spacecraft potential decreases with time. Our interpretation is confirmed in Figure 14, where we plot the spacecraft potential versus the electron and ion equivalent radii for different values of the density n, from simulations C_1 and C_3. Let us consider case C_1 (Figure 14, left) first. One can see that the equivalent radii $\mathcal{R}_{e,1}$ and $\mathcal{R}_{i,1}$ of the $n = 1$ electron and ion contours overlap almost perfectly throughout the simulation, indicating quasi-neutrality where $n = 1$. On the other hand, the curves $\mathcal{R}_{e,0.1}$ and $\mathcal{R}_{i,0.1}$ do not overlap each other for small values of ψ_{sp} (i.e., for early times), and tend to be closer together for $\mathcal{R}_{s,0.1} \gtrsim 4$, after ψ_{sp} has reached its maximum. The curves for $\mathcal{R}_{s,0.25}$ tend to be quite close to one another. From Figure 14 (left), one can infer that the quasi-neutral contactor boundary lies between $n = 1$ and $n = 0.1$, close to $n \approx 0.25$. By comparing $\mathcal{R}_{s,0.25}$ with the radius obtained by the Child-Langmuir law calculated for $I_{CL}^{sph} = I_b$ (from Figure 6 (right), plotted in Figure 14 with a dashed line), it is clear that the spacecraft potential peaks when the two curves cross. The same considerations are valid for case C_3, plotted in Figure 14 (right), where one can see that the edge of the quasi-neutral cloud is now delimited by $n \approx 0.03$.

Finally, in order to investigate the effect of the boundary condition at the outer boundary, we have performed some simulations with a bigger domain, $\rho_2 = 100$ (but keeping the same level of resolution). We recall that our simulation domain is open and therefore the total charge in the system can vary: the contactor plasma and the beam expand and at some point leave the system. Figure 15 (left) shows the spacecraft potential for Cases C_1-C_3 (solid lines are for $\rho_2 = 100$, while the dashed lines are for $\rho_2 = 50$). The curves are qualitatively similar: the spacecraft potential grows in time, peaks, and starts to decrease. The maximum of the spacecraft is larger for the bigger domain, and, as expected, more so when the initial contactor configuration is bigger. However, in all cases the spacecraft potential peaks earlier than the time where the ion front meets the boundary (which occurs at $\tau \sim 2500$ for all cases). Figure 15 (right) shows the spacecraft potential versus the electron and ion equivalent radii for different values of the density n for case C_3 (cf. Figure 14). As before, we see that the peak of the spacecraft potential is reached when the equivalent radius of the quasi-neutral plume (now for $n \approx 0.02$) meets the radius obtained by the Child-Langmuir law calculated for $I_{CL}^{sph} = I_b$.

If we compare the results of this section with those in section 3.2 for the ion beam, the role of the contactor in aiding beam emission emerges. In essence, the contactor, through its quasi-neutral cloud, mediates ion emission and enables a transition from planar geometry (which is strongly space charge limited) to a quasi-spherical emission over a larger area that is not space charge limited. For this reason the contactor mitigates the transient of the spacecraft potential and facilitates beam emission: with a sufficiently large initial contactor cloud one could ensure that the peak of the spacecraft potential remains under control.
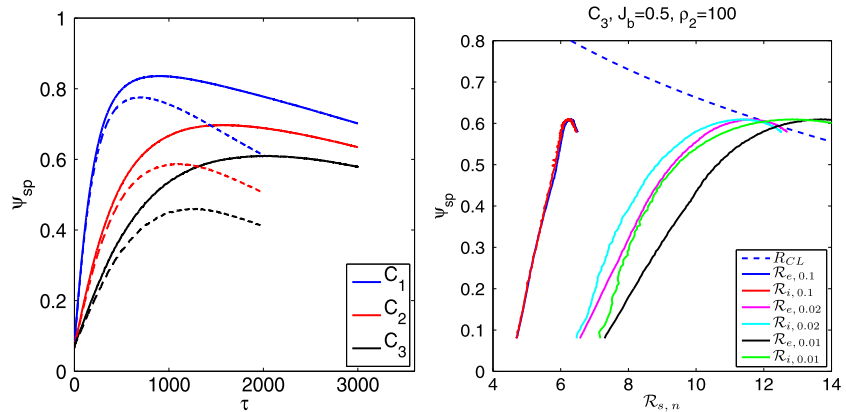
Figure 15. Simulations of contactor and beam emission: (left) spacecraft potential versus time for cases C_1-C_3 with domain outer boundary at $\rho_2 = 100$ (solid lines) and $\rho_2 = 50$ (dashed lines) and (right) spacecraft potential versus equivalent radii $\mathcal{R}_{s,n}$ for case C_3 and $\rho_2 = 100$. The radius obtained by the Child-Langmuir law in spherical geometry when $l_{CL}^{sph} = l_b = 0.093$ is plotted with a dashed line. Other parameters: $J_b = 0.5$.

3.3.3. Scaling Laws

We have also performed some parametric studies to identify scaling laws that could be of practical importance from a mission design point of view. Table 5 shows the dependence of ψ_{sp}^{max} on the contactor ion mass, all the other parameters unchanged relative to the reference case with $J_b = 0.5$ discussed in section 2.1. We have limited this study to cases C_1-C_3. We note that the initial contactor configuration obtained prior to beam emission also depends on the ion mass since lighter ions travel faster and determine larger contactor clouds. For this reason, in Table 5 we also show $\mathcal{A}_{i,10^{-6}}$ at $\tau = 0$ for each case. While the initial condition for each simulation is not the same and this is reflected in ψ_{sp}^{max}, it is evident from Table 5 that larger ion mass corresponds to larger ψ_{sp}^{max}. Attempting a least squares fit of the data gives

$$\psi_{sp}^{max} \propto \left(\frac{m_i}{m_e}\right)^{\alpha}, \quad \alpha = 0.40, \, 0.50, \, 0.57 \tag{12}$$

for C_1, C_2, and C_3, respectively. The trend in α for different cases should be attributed to the fact that the initial condition depends on the ion mass. One suspects that the scaling $\alpha = 0.4$ obtained for C_1 should be closer to reality, since for the other two cases the difference in the initial condition is bigger.

Table 6 shows ψ_{sp}^{max} varying the beam current, all the other parameters unchanged relative to our reference case. Unlike the case of Table 5, for each row in Table 6 the initial contactor configuration is the same. It is worth noting that the case $J_b = 0.25$ is qualitatively similar to $J_b = 0.5$ discussed above, while $J_b = 1$ involves some differences. In particular, for the $J_b = 1$ cases the spacecraft potential tends to an asymptotic equilibrium

Table 5. Maximum of the Spacecraft Potential ψ_{sp}^{max} and Area $\mathcal{A}_{i,10^{-6}}$ at Time $\tau = 0$ Varying the Ion Mass[a]

	$\frac{m_i}{m_e} = 918$	$\frac{m_i}{m_e} = 1836$	$\frac{m_i}{m_e} = 3672$	Best fit	Simulation
ψ_{sp}^{max}	0.58	0.78	1.01	$\propto \left(\frac{m_i}{m_e}\right)^{0.40}$	C_1
ψ_{sp}^{max}	0.40	0.59	0.80	$\propto \left(\frac{m_i}{m_e}\right)^{0.50}$	C_2
ψ_{sp}^{max}	0.30	0.46	0.66	$\propto \left(\frac{m_i}{m_e}\right)^{0.57}$	C_3
$\mathcal{A}_{i,10^{-6}}(\tau = 0)$	17.2	10.6	6.7		C_1
$\mathcal{A}_{i,10^{-6}}(\tau = 0)$	172.1	98.1	53.3		C_2
$\mathcal{A}_{i,10^{-6}}(\tau = 0)$	515.2	294.2	155.3		C_3

[a]All the other parameters are unchanged relative to the reference case discussed in section 2.1.

Table 6. Maximum of the Spacecraft Potential ψ_{sp}^{max} Varying the Beam Current, All the Other Parameters Are Unchanged Relative to the Reference Case Discussed in Section 2.1 as in Table 5

	$J_b = 0.25$	$J_b = 0.5$	$J_b = 1$	Best Fit	Simulation
ψ_{sp}^{max}	0.37	0.78	1.97	$\propto J_b^{1.20}$	C_1
ψ_{sp}^{max}	0.27	0.59	1.37	$\propto J_b^{1.17}$	C_2
ψ_{sp}^{max}	0.21	0.46	1.09	$\propto J_b^{1.19}$	C_3

(cf. Figure 11) where $I_i = I_b$ and there is no electron tail current from the contactor. The least squares fit of the data in Table 6 gives

$$\psi_{sp}^{max} \propto J_b^{1.2} \tag{13}$$

essentially independent of the initial condition.

3.3.4. A Rough Estimate of ψ_{sp}^{max}

It would be useful to derive a simple estimate for ψ_{sp}^{max}. Following the discussion above, in order to do this one needs to estimate the expansion of the quasi-neutral contactor and evaluate when its equivalent radius matches the radius where the Child-Langmuir current $I_{CL}^{sph} = I_b$ (Figure 6, right). We label this radius as R_{CL} and emphasize its dependence on ψ_{sp}, I_b and m_i/m_e. If we assume that the result in Figure 10 is 'universally' valid, that is $d\mathcal{A}_{i,QN}/dt = V_p$ (where the subscript QN labels the density contour corresponding to the edge of the quasi-neutral contactor), it is easy to obtain the evolution of the equivalent radius

$$\mathcal{R}_{i,QN} = \sqrt{\left(\mathcal{R}_{i0,QN}\right)^2 + \frac{V_p}{\pi}\tau}, \tag{14}$$

where $\mathcal{R}_{i0,QN} = \mathcal{R}_{i,QN}(\tau = 0)$. Equation (14) can be expressed in terms of ψ_{sp} by using equation (11) for τ. Finally the maximum of the spacecraft potential can be estimated by solving the following nonlinear equation

$$\sqrt{\left(\mathcal{R}_{i0,QN}\right)^2 + \frac{4\mathcal{R}_{i0,10^{-6}}V_p}{I_b}\psi_{sp}^*} = R_{CL}\left(\psi_{sp}^*, I_b, \frac{m_i}{m_e}\right) \tag{15}$$

where $\mathcal{R}_{i0,10^{-6}} = \mathcal{R}_{i,10^{-6}}(\tau = 0)$. Obviously one must know the properties of the contactor prior to beam emission to use equation (15). We have applied expression (15) to cases C_1 and C_3 of Table 6. For C_1, $\mathcal{R}_{i0,10^{-6}} = 2.6$ (Table 4) and $\mathcal{R}_{i0,QN} = \mathcal{R}_{i0,0.25} = 1.7$ (Figure 14), leading to $\psi_{sp}^* = 0.53, 0.92, 1.57$ for $J_b = 0.25, 0.5, 1$. For C_3, $\mathcal{R}_{i0,10^{-6}} = 13.7$ and $\mathcal{R}_{i0,QN} = \mathcal{R}_{i0,0.03} = 6.0$, leading to $\psi_{sp}^* = 0.33, 0.59, 1.02$ for $J_b = 0.25, 0.5, 1$. In both cases the relative error between the prediction of equation (15) and the PIC simulations is at most $\sim 50\%$.

4. Conclusions

In this paper we have performed PIC simulations to investigate the conditions for which a high-voltage electron beam can be emitted by a spacecraft without incurring dramatic spacecraft charging problems. We have investigated several settings, including the idea of balancing the electron beam with an ion beam of equal current, and explored the role of a (neutral) contactor plasma injected prior and with the electron beam. While the ion beam strategy cannot work because of space charge problems that effectively prevent the ion beam from leaving the spacecraft, we have shown that the contactor is critical in enabling electron beam emission. In particular, our most important result is that the contactor regulates ion emission by spreading it over a larger area and effectively inducing a transition from a planar geometry emission (cf. the ion beam, strongly space charge limited) to a quasi-spherical geometry emission (not space charge limited).

We have shown that the contactor controls the transient of the spacecraft potential induced by beam emission. Specifically, for $I_b < I_i$ the spacecraft potential initially grows and later decays in time. We have explained this nonmonotonic behavior in terms of the expansion of the quasi-neutral part of the contactor towards conditions that do not violate the Child-Langmuir law. Moreover, we have shown that larger contactor areas prior to beam emission mitigate the transient and result in lower peaks of the spacecraft potential. This is consistent with a simple picture where the combined capacitance of the spacecraft plus the contactor plasma cloud

increases, and implies that a sufficiently large contactor cloud area can ensure that the peak of the spacecraft potential remains within acceptable bounds.

We have also presented the scaling laws of the maximum of the spacecraft potential varying the contactor ion mass, $\psi_{sp}^{max} \propto \left(\frac{m_i}{m_e}\right)^{0.4}$, and the electron beam current, $\psi_{sp}^{max} \propto I_b^{1.2}$, which are of practical importance from a mission design point of view.

The results presented in this paper might also help shed some light on past experimental results. For instance, *Katz et al.* [1994] discuss experiments performed during the ST-45 Atlas-1 mission where keV electron beams with currents up to 0.8 A operated in conjunction with a plasma contactor unit that generated 2 A of Xenon ions. These experiments were conducted in the ionosphere, at 300 km altitude, where the return current from the plasma can be significant and is influenced by the cross-field conductivity. *Katz et al.* [1994] report that the data showed no evidence of spacecraft charging or beam return, but it was unclear whether the contactor current was carried by electrons flowing in from the ionosphere or by ions flowing from the contactor out to the ionosphere. Although it is not possible to make a direct comparison, our results suggest that is the latter scenario that maintains spacecraft charging under control when the background return current is not enough.

In light of the renewed interest for beam experiments in space [cf. *National Research Council*, 2012], for instance to actively probe magnetic field line connectivity over vast regions of near-Earth space, our results indicate that operating the contactor and the electron beam simultaneously (in a regime of higher contactor current) offers a possible pathway to substantially mitigate spacecraft charging problems even in a tenuous, realistic magnetosphere.

References

Birdsall, C., and A. Langdon (1985), *Plasma Physics via Computer Simulation*, McGraw-Hill, New York.

Borovsky, J. E., D. J. McComas, M. F. Thomsen, J. L. Burch, J. Cravens, C. J. Pollock, T. E. Moore, and S. B. Mende (2000), Magnetosphere-Ionosphere Observatory (MIO): A multisatellite mission designed to solve the problem of what generates auroral arcs, *Eos Trans. AGU*, *79*(45), F744.

Child, C. D. (1911), Discharge from hot CaO, *Phys. Rev.*, *32*, 492–511.

Cohen, H. A., A. L. Chesley, T. Aggson, M. S. Gussenhoven, R. C. Olsen, and E. C. Whipple (1980a), A comparison of three techniques of discharging satellites, *Proceedings of the Third Spacecraft Charging and Technology Conference*, 888–893, US Air Force Academy, Colorado Springs, Colo.

Cohen, H. A., et al. (1980b), P78-2 satellite and payload responses to electron beam operations on March 30, 1979, *Proceedings of the Third Spacecraft Charging and Technology Conference,* 509–559, US Air Force Academy, Colorado Springs, Colo.

Comfort, R. H., T. E. Moore, P. D. Craven, C. J. Pollock, F. S. Mozer, and W. S. Williamson (1998), Spacecraft potential control by the Plasma Source Instrument on the POLAR satellite, *J. Spacecraft Rockets*, *35*, 845–849.

DeForest, S. E. (1972), Spacecraft charging at synchronous orbit, *J. Geophys. Res.*, *77*, 651–659.

Delzanno, G. L., and X. Z. Tang (2014), Charging and heat collection by a positively charged dust grain in a plasma, *Phys. Rev. Lett.*, *113*(3), 035002.

Delzanno, G. L., E. Camporeale, J. D. Moulton, J. E. Borovsky, E. A. MacDonald, and M. F. Thomsen (2013), CPIC: A curvilinear particle-in-cell code for plasma-material interaction studies, *IEEE Trans. Plasma Sci.*, *41*(12), 3577–3587.

Delzanno, G. L., J. E. Borovsky, M. F. Thomsen, and J. D. Moulton (2015), Future beam experiments in the magnetosphere with plasma contactors: The electron collection and ion emission routes, *J. Geophys. Res. Space Physics*, doi:10.1002/2014JA020683.

Gussenhoven, M. S., H. A. Cohen, D. A. Hardy, W. J. Burke, and A. L. Chesley (1980), Analysis of ambient and beam particle characteristics during the ejection of an electron beam from a satellite in near-geosynchronous orbit on March 30, 1979, *Proceedings of the Third Spacecraft Charging and Technology Conference*, 642–664, US Air Force Academy, Colorado Springs, Colo.

Hallinan, T. J., H. C. Stenbaek-Nielsen, and J. R. Winckler (1978), The Echo 4 electron beam experiment: Television observation of artificial auroral streaks indicating strong beam interaction in the high-latitude magnetosphere, *J. Geophys. Res.*, *83*, 3263–3272.

Hastings, D., and H. Garrett (1996), *Spacecraft-Environment Interactions*, Cambridge Univ. Press, Cambridge.

Hendrickson, R. A., R. W. McEntire, and J. R. Winckler (1975), Echo 1: An experimental analysis of local effects and conjugate return echoes from an electron beam injected into the magnetosphere by a souning rocket, *Planet. Space Sci.*, *23*, 1431.

Huang, C. Y., W. J. Burke, D. A. Hardy, M. P. Grough, D. G. Olsen, L. C. Gentile, B. E. Gilchrist, C. Bonifazi, W. J. Raitt, and D. C. Thompson (1998), Cerenkov emissions of ion acoustic-like waves generated by electron beams emitted during TSS 1R, *Geophys. Res. Lett.*, *25*, 721–724.

Katz, I., J. N. Barfield, J. L. Burch, J. A. Marshall, W. C. Gibson, T. Neubert, W. T. Roberts, W. W. L. Taylor, and J. R. Beattie (1994), Interactions between the space experiments with particle accelerators, plasma contactor, and the ionosphere, *J. Spacecraft Rockets*, *31*, 1079–1084.

Krehbiel, P. R., M. Brook, and R. A. McCrory (1979), An analysis of the charge structure of lightning discharges to ground, *J. Geophys. Res.*, *84*, 2432–2456.

Langmuir, I., and K. B. Blodgett (1924), Current limited by space charge between concentric spheres, *Phys. Rev.*, *23*, 49–59.

Lau, Y. Y. (2001), Simple theory for the two-dimensional child-langmuir law, *Phys. Rev. Lett.*, *87*, 278301.

Lavergnat, J. (1982), The French-Soviet experiment ARAKS: Main results, in *Artificial Particle Beams in Space Plasma Studies*, edited by B. Grandal, pp. 87, Plenum, New York.

Lieberman, M. A., and A. J. Lichtenberg (2005), *Principles of Plasma Discharges and Materials Processing*, Wiley Interscience, Hoboken, N. J.

MacDonald, E. A., J. E. Borovsky, B. Larsen, and E. Dors (2012), A science mission concept to actively probe magnetosphere-ionosphere coupling. *Decadal Survey in Solar and Space Physics papers*.

Mandell, M. J., V. A. Davis, D. L. Cooke, A. T. Wheelock, and C. J. Roth (2006), Nascap-2k spacecraft charging code overview, *IEEE Trans. Plasma Sci.*, *34*(5), 2084–2093.

Matéo-Vélez, J.-C., et al. (2012), SPIS Science: modelling spacecraft cleanliness for low-energy plasma measurement, *Proceedings of the 12th Spacecraft Charging and Technology Conference,* Kitakyushu, Japan.

Muranaka, T., et al. (2008), Development of multi-utility spacecraft charging analysis tool (MUSCAT), *IEEE Trans. Plasma Sci.*, *36*(5), 2336–2349.

Myers, N. B., W. J. Raitt, A. B. White, P. M. Banks, B. E. Gilchrist, and S. Sasaki (1990), Vehicle charging effects during electron beam emission from the CHARGE-2 experiment, *J. Spacecraft Rockets*, *27*, 25–37.

National Research Council (2012), *Solar and Space Physics: A Science for a Technological Society*, National Academies Press, Washington, D. C.

Nemzek, R. J., and J. R. Winckler (1991), Electron beam sounding rocket experiments for probing the distant magnetosphere, *Phys. Rev. Lett.*, *67*, 987–990.

Nemzek, R. J., P. R. Malcolm, and J. R. Winckler (1992), Comparison of Echo 7 field line length measurements to magnetospheric model predictions, *J. Geophys. Res.*, *97*, 1279–1287.

Neubert, T., and B. E. Gilchrist (2004), Relativistic electron beam injection from spacecraft: Performance and applications, *Adv. Space Res.*, *34*, 2409–2412.

Olsen, R. C. (1985), Experiments in charge control at geosynchronous orbit – ATS-5 and ATS-6, *J. Spacecraft Rockets*, *22*, 254–264.

Pellat, R., and R. Z. Sagdeev (1980), Concluding remarks on the ARAKS experiments, *Ann. Geophys.*, *36*, 443–446.

Prech, L., Z. Nemecek, J. Safrankova, J. Simunek, V. Truhlik, and N. M. Shutte (1995), Response of the electron energy distribution to an artificially emitted electron bea: APEX experiment, *Adv. Space Res.*, *15*(12), 33–36.

Prech, L., Z. Nemecek, J. Safrankova, and A. Omar (2002), Actively produced high-energy electron bursts within the magnetosphere: The APEX project, *Ann. Geophys.*, *20*, 1529–1538.

Raitt, W. J., A. B. White, A. C. Fraser-Smith, B. E. Gilchrist, and T. J. Hallinan (1995), VLF wave experiments in space using a modulated electron beam, *J. Spacecraft Rockets*, *32*, 670–679.

Roussel, J.-F., F. Rogier, G. Dufour, J.-C. Mateo-Velez, J. Forest, A. Hilgers, D. Rodgers, L. Girard, and D. Payan (2008), Spis open-source code: methods, capabilities, achievements, and prospects, *IEEE Trans. on Plasma Sci.*, *36*(5), 2360–2368.

Rubin, A. G., H. A. Cohen, D. A. Hardy, M. F. Tautz, and N. A. Saflekos (1980), Computer simulation of spacecraft charging on SCATHA, *Proceedings of the Third Spacecraft Charging and Technology Conference*, 632–641, US Air Force Academy, Colorado Springs, Colo.

Schmidt, R., et al. (1995), Results from active spacecraft potential control on the Geotail spacecraft, *J. Geophys. Res.*, *100*, 17,253–17,259.

Swanson, R. L., J. E. Steffen, and J. R. Winckler (1986), The effect of strong pitch angle scattering on the use of artificial auroral streaks for echo detection – ECHO 5, *Planet. Space Sci.*, *34*, 411–427.

Torkar, K., et al. (2001), Active spacecraft potential for Cluster – implementation and first results, *Ann. Geophys.*, *19*, 1289–1302.

Uman, M. A. (1987), *The Lightning Discharge*, Academic Press, Orlando, Fla.

Wang, J., and S. T. Lai (1997), Virtual anode in ion beam emissions in space: Numerical simulations, *J. Spacecraft Rockets*, *6*, 829–836.

Whipple, E. C. (1981), Potentials of surfaces in space, *Rep. Prog. Phys.*, *44*, 1197.

Wilhelm, K., W. Bernstrein, and B. A. Whalen (1980), Study of electric fields parallel to the magnetic lines of force using artificially injected energetic electrons, *Geophys. Res. Lett.*, *7*, 117–120.

Winckler, J. R. (1980), The application of artificial electron beams to magnetospheric research, *Rev. Geophys.*, *18*(3), 659–682.

Winckler, J. R. (1992), Controlled experiments in the Earth's magnetosphere with artificial electron beams, *Rev. Mod. Phys.*, *64*, 859–871.

Zhulin, I. A., A. V. Kustov, M. V. Uspensky, and T. V. Miroshnikova (1980), Radar observations of the overdense ionospheric ionization created by the artificial electron beam in the "Zarnitza-2" experiment, *Ann. Geophys.*, *36*, 313–318.